Nanoscale Electrocatalysis of Hydrazine Electro-Oxidation at Blistered Graphite Electrodes

Sharel P. E,[†] *Yang-Rae Kim,*[†,§] *David Perry,*[†, ‡] *Cameron L. Bentley,*[†] *and Patrick R. Unwin.*[*†]

[†]Department of Chemistry, [‡]MOAC Doctoral Training Centre, University of Warwick, Coventry, CV4 7AL, United Kingdom

[§]Department of Chemistry, Kwangwoon University, Seoul 01897, Republic of Korea

*To whom correspondence should be addressed. E-mail: p.r.unwin@warwick.ac.uk

ABSTRACT

There is great interest in finding and developing new, efficient and more active electrocatalytic materials. Surface modification of highly oriented pyrolytic graphite (HOPG), through the introduction of surface "blisters", is demonstrated to result in an electrode material with greatly enhanced electrochemical activity. The increased electrochemical activity of these blisters, which are produced by electro-oxidation in $HClO_4$, is revealed through the use of scanning electrochemical cell microscopy (SECCM), coupled with complementary techniques (optical microscopy, FE-SEM, Raman spectroscopy, and AFM). The use of a linear sweep voltammetry (LSV)-SECCM scan regime allows for dynamic electrochemical mapping, where a voltammogram is produced at each pixel, from which movies consisting of spatial electrochemical currents, at a series of applied potentials, are produced. The measurements reveal significantly enhanced activity at blisters when compared to the basal planes, with a significant cathodic shift of the onset potential for the hydrazine electro-oxidation reaction. The improved electrochemical activity of the hollow structure of blistered graphite could be explained by the increased adsorption of protonated hydrazine at oxygenated defect sites, the ease of ion-solvent intercalation/de-intercalation, and the susceptibility to N_2 nanobubble attachment (as a product of the reaction). This study highlights the capability of electrochemistry to tailor the surface structure of graphite and presents a new electrocatalyst for hydrazine electro-oxidation.

KEYWORDS: Graphite, Nanoelectrochemistry, Electrocatalysis, Scanning Electrochemical Cell Microscopy, Hydrazine Oxidation

INTRODUCTION

There has been an intense push towards efficient and inexpensive alternatives to noble-metal electrocatalysts (*i.e.* platinum and ruthenium) for a wide range of applications.[1-4] Great efforts have been made in developing non-noble metals catalysts through means of surface modification, doping, and alloying,[5, 6] with varying degrees of success.[7] Beyond metals, carbon-based materials, which have mainly been used as supports for electrocatalysts,[8, 9] are receiving increasing attention as electrocatalysts in their own right.[7, 10-12] Carbon is an attractive proposition, due to the possibility of modification by doping and surface functionalization in a wide variety of ways.[13-15] This is particularly true of graphite, which comprises stacked graphene layers with weak van der Waals force present between the layers.[7]

While outer sphere redox processes, and some more complex electron-proton coupled processes, occur readily at the basal structure of graphite,[16-21] electrocatalytic (bond-breaking) reactions often require additional efforts to promote the electrochemical activity. There are 3 broad, and somewhat interrelated, approaches and effects to consider: (i) selective doping of sp^2 materials by various heteroatoms (*e.g.* N,[22] B,[23] S,[24] and P[25]); (ii) surface modification with different functional groups by chemical oxidation, or grafting[26, 27] and (iii) defects, which may promote electrocatalysis.[28, 29] An interesting way to introduce defects is by the intercalation of anions (ClO_4^-, NO_3^-, and SO_4^{2-}) during the electrochemical oxidation of sp^2 carbon materials (*e.g.* graphite), which ultimately leads to delamination, followed by fracturing into a bubble-like blister structure (hollow interior), that is presented on the graphite surface.[30-32] These are interesting structures, but their electrocatalytic properties have not been widely studied.

Herein, we investigate the electrocatalytic activity of blisters on an HOPG surface for hydrazine (N_2H_4) oxidation. Hydrazine is a high-energy fuel molecule, which has been investigated for the development of high power density direct hydrazine-air fuel cells.[33] Separately, hydrazine is a carcinogenic and hepatotoxic compound, which affects glutathione levels in the brain and liver,[34] and a such, the development of strategies for hydrazine detection is an important task, with electrochemical detection showing promise.[35, 36]

Electrochemical measurements with high spatial and temporal resolution, can provide major insights into the activity of functional electrode materials, and our group has shown that scanning electrochemical cell microscopy (SECCM) is particularly promising for revealing nanoscale electrochemical activity and topographical information at a variety of substrates. SECCM is especially powerful when combined with other forms of microscopy, applied to the same area as electrochemical mapping, in a correlative approach.[37-40] In this paper, we use a hopping voltammetric mode SECCM regime, in which a linear sweep voltammetry (LSV) measurement is performed at each location (pixel) of the defined scan area. These data can be processed to provide electrochemical activity maps, comprising hundreds of spatially-resolved current measurements as a function of potential, that can be played back as a movie, from which potential-resolved snapshots can be extracted, and from which current-voltage curves, Tafel analysis, etc. can be performed at individual pixels. The use of complementary microscopy techniques applied to the same area, including optical microscopy, scanning electron microscopy (SEM), atomic force microscopy (AFM), and micro-Raman, permits a detailed investigation into the structure-activity relationships of nanoscale features.

METHODS

Materials. All chemicals were used as received. Electrolyte solutions were prepared freshly using deionized water produced by a Purite Select HP system (resistivity of 18.2 MΩ cm at 25 °C) and $HClO_4$ (70 %, Sigma Aldrich). 5 mM Hydrazine (64 %, Acros Organics) was prepared in 0.1 M phosphate-buffered solution (PBS, pH 7.4). PBS was prepared in house from sodium phosphate dibasic heptahydrate ($Na_2HPO_4{\cdot}7H_2O$, Sigma-Aldrich, 98-102 %) and sodium dihydrogen orthophosphate dihydrate ($NaH_2PO_4{\cdot}2H_2O$, Fisher Scientific, 99-101 %). Pd wire (99.9 %, 0.25 mm diameter, Alfa Aesar) was used to make Pd-H_2 quasi-reference counter electrodes (QRCEs) and quasi-reference electrodes as described elsewhere.[38] All reported potentials are against the reversible hydrogen electrode ($E_{\mathrm{Pd-H_2}} = 50$ mV $vs.$ RHE).[41] A high-quality AM-grade HOPG sample was used as a substrate, originating from Dr. A. Moore, Union Carbide (now GE Advanced Ceramics), and kindly provided by Prof. Richard L. McCreery (University of Alberta, Canada).

Droplet experiments. The electrochemical formation of blisters was carried out in a 3-electrode setup, with freshly cleaved AM-grade HOPG acting as the working electrode (WE). Electrical contact to the WE was made via conductive Ag paint applied to the electrometer head unit. A drop of electrolyte solution (~10 µL of 0.1 M $HClO_4$, ~ 4 mm dia.) was placed on the HOPG surface (Figure 1a). A Pt wire (99.95 %, 0.6 mm diameter, Alfa Aesar) was used as a counter electrode (CE) and Pd-H_2 wire acted as a quasi-reference electrode. These were positioned within the droplet of solution.[18, 42] The electrochemical measurements were performed with a CHI 730 electrochemical workstation (CH Instruments, TX, USA).[43, 44]

Hopping SECCM-LSV experiments. Borosilicate theta (dual channeled) capillaries (ID = 1.0 mm, OD = 1.5 mm, Harvard Apparatus, UK) were pulled using a laser pipette puller (P-2000, Sutter

Instrument Co., USA) to produce nanopipettes with a diameter of around 400 nm (200 nm each channel). Nanopipettes were silanized using dichlorodimethylsilane (>99 %, Acros) to produce a hydrophobic outer surface, whilst Ar gas was flowed through to prevent any internal silanization. This process ensured a confined aqueous meniscus contact during SECCM experiments.[37]

A schematic illustrating the hopping SECCM method is shown in Figure 1b. Briefly, a dual barreled nanopipette, filled with 5 mM N_2H_4 solution as well as a Pd-H_2 wire in each channel, which act as QRCEs, functions as both a conductimetric and voltammetric cell. The nanopipette was approached towards the surface of the HOPG substrate until the meniscus made contact (without contact from the nanopipette itself). The nanopipette was used to make a series of measurements by landing the meniscus at a set of predefined locations. Electrolyte residues from the SECCM meniscus (*vide infra*) were visualized after experiments using field emission-scanning electron microscopy (FE-SEM) (Supra 55-VP, Zeiss) to provide key information about the meniscus size and location. The hopping distance between each pixel was 2 μm to avoid overlap of the probed areas (~ 900 nm in dia.).

High precision control of the meniscus contact was achieved by applying a bias voltage (V_2, 200 mV) between the two QRCEs to produce a direct ion current (I_{IC}) across the meniscus. The nanopipette was oscillated perpendicular to the surface (267 Hz, 14 nm peak-to-peak amplitude) to induce an alternating current (AC) component of the ionic current signal between two barrels as the meniscus came into contact with the surface. The AC signal, at the generated oscillation frequency, was detected using a lock-in amplifier (SR380, Stafford Research System) and the resulting AC response served as the feedback signal for positioning the nanopipette at a set distance from the electrode surface. The working electrode potential (E_s) was $-(V_1 + V_2/2)$ *vs.* Pd-H_2, against which all the electrochemical currents of the substrate (I_{EC}) were measured using a

custom built, high-sensitivity, current-to-voltage converter. The voltammetric scan rate was 500 mV s^{-1}, applied at each point of meniscus contact, giving a spatial array of voltammograms. Data analysis was performed in Matlab (R2014b, Mathworks Inc.) to provide I_{EC} spatial maps over a set of potentials which could also be presented as movies (see, for example, Supporting Information, Movie S2 and S3, which are discussed later).[37, 45]

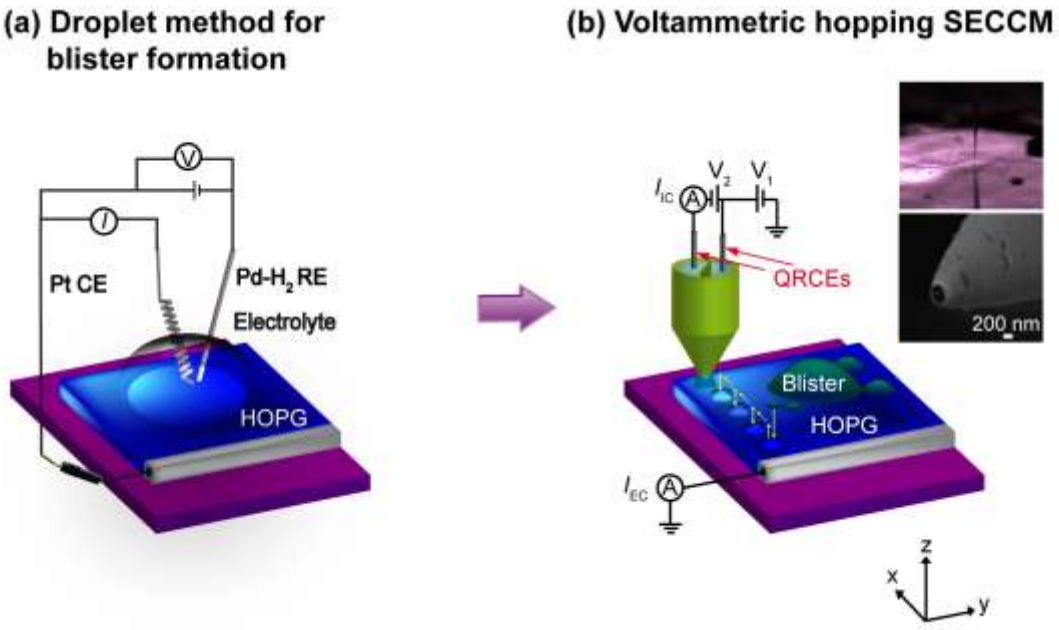

Figure 1. Experimental setup for (a) blister formation on HOPG using the droplet method[43, 44] (0.1 M $HClO_4$) and (b) nanoscopic electrocatalytic measurement using voltammetric hopping mode SECCM. For SECCM, a bias voltage (V_2) was applied between two QRCEs and the resulting ion conductance current (I_{IC}) was measured and used for nanopipette positioning. A substrate voltage (V_1) was applied to one of the QRCEs to control the working electrode potential ($E_s = -(V_1 + V_2/2)$ *vs*. Pd-H_2), and the working electrode current (I_{EC}) was measured. Small amounts of residue were left on the surface after withdrawing the nanopipette from each position, which aided location identification by other techniques. The arrows show the movement of the nanopipette.

Micro-Raman and AFM experiments. Micro-Raman spectroscopy (InVia Reflex Raman, Renishaw, UK) fitted with a solid state 532 nm laser and a 50× lens was used to determine the

nature of the treated HOPG surface. For Raman mapping, the laser beam was raster-scanned across the area of interest, with spectra obtained every 0.8 µm and 1.0 µm over two predefined areas. Tapping mode AFM imaging of the HOPG was carried out in air (Innova, Veeco-Bruker).

RESULTS AND DISCUSSION

Surface Blistering of HOPG. Perchlorate (ClO_4^-) is known to intercalate into HOPG at anodic potentials, with the extent of intercalation depending on the potential applied and exposure time.[30, 42, 46] Three consecutive cyclic voltammograms were performed on freshly cleaved HOPG in 0.1 M $HClO_4$, with start and reverse potentials of 0.15 V_{RHE} and 2.35 V_{RHE}, respectively (25 mV s^{-1}). The insertion and removal of ClO_4^- ions is manifest as redox peaks, as shown in Figure 2a and the inset. For the first anodic scan, small oxidation peaks at 1.95 V_{RHE} (I), 2.12 V_{RHE} (II), and 2.22 V_{RHE} (III) are similar to those seen previously that were attributed to three different anion intercalation stages.[30-32, 47] A broad reduction peak at ca. 1.7 V_{RHE} on the reverse scan corresponds to de-intercalation of ClO_4^- from the graphite. The current magnitudes for the redox peaks increased and progressively shifted towards more cathodic values, as the number of cycles increased, which can be attributed to more facile anion intercalation/de-intercalation.

On the anodic scan, ClO_4^- ions, along with solvent and acid molecules, are incorporated into the graphite lattice through defect sites, overcoming the weak van der Waals' interactions between the graphene layers.[32, 48] The intercalation process[31] can be described by:

$$C_x + ClO_4^- + yHClO_4 \rightleftharpoons C_x^+ClO_4^-(HClO_4)y + e^- \quad (1)$$

Irreversible side reactions involving graphite oxide formation and water electrolysis may also occur at anodic potentials. These reactions contribute to the anodic currents at relatively high

positive potentials.[46] Surface quinone-hydroquinone redox reactions[49] may also occur at electrochemically-functionalized graphite surface involving the alcohol and carbonyl groups that are formed at edge planes and defect sites.

Figure 2b shows an FE-SEM image of HOPG after oxidation in $HClO_4$ for three potential cycles (as defined above). The image reveals the formation of blisters along grain boundaries. The magnified FE-SEM image (Figure 2c) shows large blisters of irregular shapes, aligned along the boundaries with small blisters extending to the surrounding grain boundaries, consistent with previous studies.[30] The mechanism of blister formation on HOPG is shown schematically in Figure 2d.[30-32] Anion intercalation starts close to, or at, surface defects (Figure 2d (1)). Intercalation of anions (ClO_4^-) first expands the interlayer gap for efficient intercalation of the solvent molecules into the graphite lattice during the anodic scan (Figure 2d (2)). Figure 2d (3) shows gas evolution (*e.g.* O_2 formation) from side reactions, occurring concurrently with the production of electrochemically generated graphite oxide. The mechanical stress, originating from the gas evolution, in particular, induces surface blistering on HOPG. De-intercalation of anion occurs during the reverse scan (Figure 2d (4)).

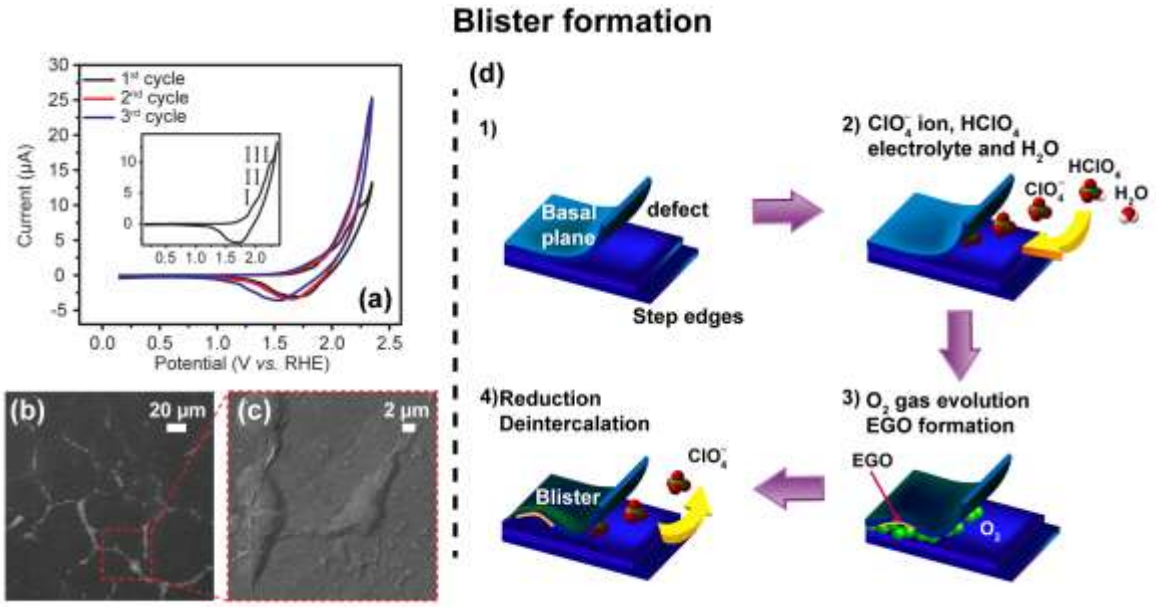

Figure 2. (a) Three consecutive voltammograms recorded at HOPG in 0.1 M $HClO_4$ (25 mV s^{-1}). Peak positions on the potential scale (inset figure) are mentioned in the text. (b and c) Corresponding FE-SEM images recorded on a blistered region of HOPG after the measurement in (a). (d) Schematic depicting the formation of a blister on HOPG.[30-32] 1) The basal plane and surface defects (step edges and grain boundaries) on an HOPG electrode, prior to electro-oxidation in 0.1 M $HClO_4$ solution. 2) Intercalation of ClO_4^- ions occurs along with the intercalation of $HClO_4$ and H_2O at defect sites during the anodic scanning of the electrode potential. 3) At more anodic potentials (and/or more extensive electro-oxidation times), blister formation occurs due to the mechanical stress produced, for example, by gas evolution. The orange colored area represents electrochemically formed graphite oxide. 4) Ions de-intercalate during the reverse scan (reduction reaction), leaving behind the blister.

Characterization of Surface Blisters on HOPG Using AFM and Raman Microscopy. A typical AFM image of AM-grade HOPG recorded prior to electrochemical cycling in 0.1 M $HClO_4$ is shown in Figure 3a. The HOPG surface is characterized by extensive flat terraces, with a few step edges clearly visible. The HOPG surface is dramatically changed after performing three initial consecutive voltammetric cycles in 0.1 M $HClO_4$ (same conditions as Figure 2a). Figure 3b

shows two small blisters of circular shape, ca. 1.2 µm across and 10 – 14 nm in height (Figure 3d). Figure 3c shows a mixture of small and large blisters of irregular shape, ranging from 0.5 – 5 µm across and 10 – 90 nm in height (Figure 3e). The elongated shape of blisters could be due to the blister formation along the grain boundaries and extension in those directions, which then results in several smaller blisters merging. Mechanical forces originating from gas evolution in the anodic oxidation process is known to promote blister growth.[31]

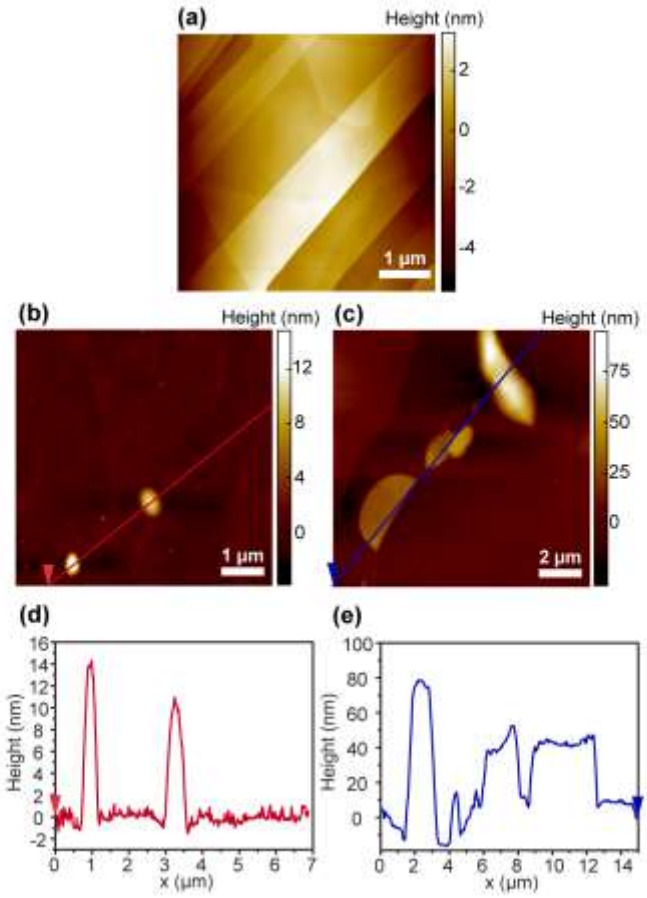

Figure 3. Typical AFM images of AM HOPG (a) before and after (b and c) voltammetric cycling 0.1 M $HClO_4$ (conditions as Figure 2a), leading to surface blistering. (d and e) Corresponding height cross sections of surface blistered regions. Note the different height scale bars.

Figure 4a(i) and b(i) show optical micrographs of two "blistered" areas on HOPG. Within these two regions are areas with basal planes and blisters, and these were analyzed with micro-Raman spectroscopy in terms of *D* band intensity (Figures 4a(ii) and 4b(ii)) and *G*/*D* ratio (Figures 4a(iii) and 4b(iii)). The micro-Raman spectra in Figures 4a(iv-vi) and b(iv-vi) were normalized with respect to the intensity of the second-order double resonance (2*D*) at 2710 cm^{-1} to permit easy comparison. The *D*-peak at 1350 cm^{-1} originates from the breakup of hexagonal sp^2 carbon atoms in the graphitic planes.[50] The Raman maps in Figures 4a(ii) and b(ii) show a higher intensity of the *D*-peak at blisters that are aligned along the grain boundaries. Corresponding micro-Raman spectra of the *D*-peak intensity for the surface blistered region increases by ca. 360 % (Figure 4a(iv and vi) and ca. 870 % (Figure 4b(iv and vi)) relative to the basal plane region. Oxidation of HOPG in 0.1 M $HClO_4$ above 1.5 V evidently caused damage to the graphite lattice as indicated by the increased intensity of the *D*-peak.[46, 51] The intense line at 1565-1595 cm^{-1} is assigned to the *G*-peak, which is also indicative of sp^2 carbon.[52] The *G*-peak in Figures 4 a(iv-vi) show little, or no difference between the blister and basal planes, but the *G*-peak bands in Figures 4 b(iv and vi) are significantly broader than usual. This can be attributed to an electrochemically formed graphite oxide region, produced during the anodic oxidation process, that varies across different regions of the "blistered" HOPG, with the broader *G*-band response caused by a thicker electrochemically formed graphite oxide film.[53] Typically, electrochemically formed graphite oxide films contain many anionic sites and are highly permeable to small molecules.[54]

The same scenario is apparent for the intensity of the *G*-peak with respect to the intensity of the *D*-peak *i.e.* (i_G /i_D), which is often used for the evaluation of the defect density in graphite.[50] Clearly, the value of i_G /i_D decreases in the blistered region. It should be noted that blisters were found only inside the contact area of the droplet at the surface of the HOPG substrate in Figures

2b, indicating that they were generated by the electrochemical process. Thus, these results show that the electrochemical generation of graphitic blisters leads to a considerable alteration of local structure.

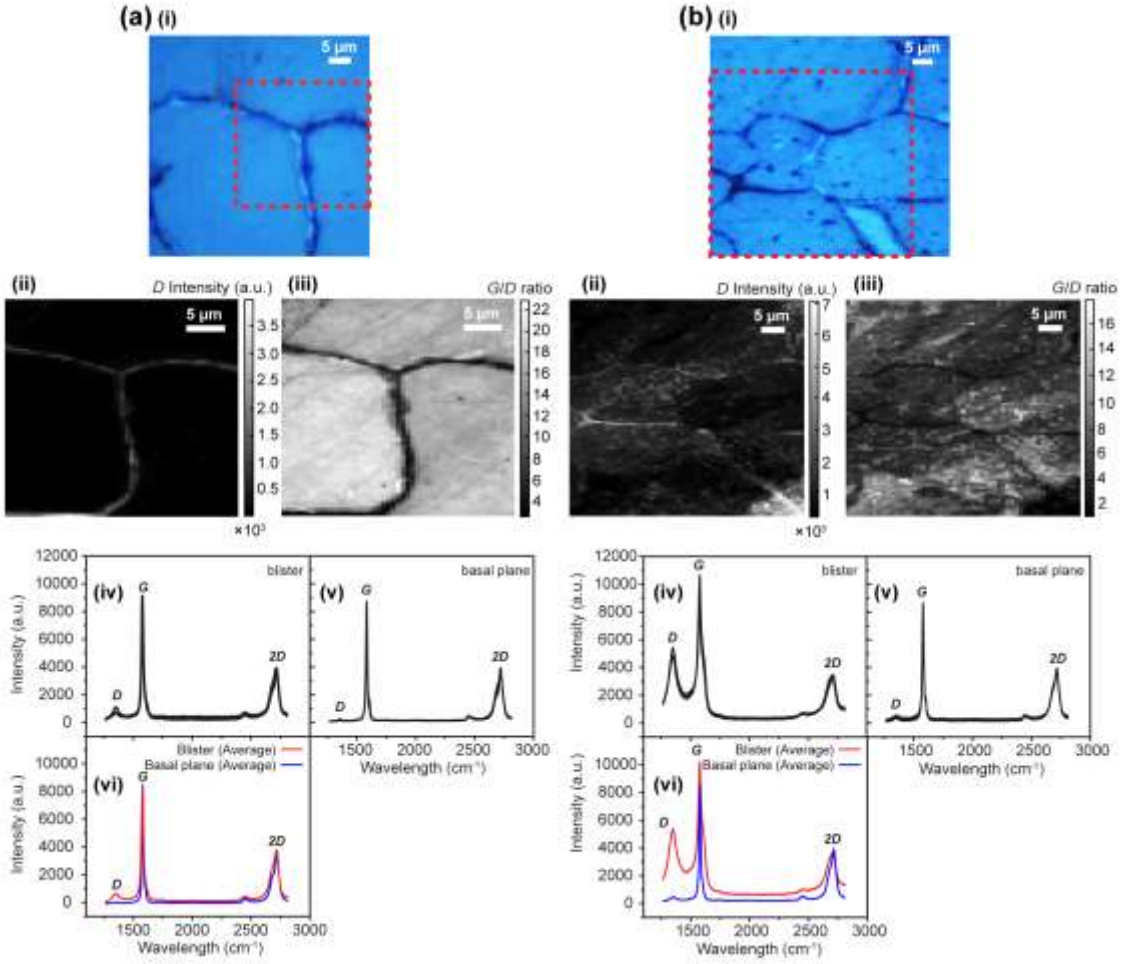

Figure 4. Optical micrographs (i) of two surface blistered regions (a and b) with corresponding micro-Raman maps of: (ii) i_D, and (iii) i_G/i_D ratio, along with individual Raman spectra at (iv) blistered and (v) basal plane regions of an electrochemically-treated HOPG surface. (vi) Averaged-spectra (n = 3 – 5) of the surface blistered region (red) and basal plane (blue) of the treated HOPG surface.

SECCM Imaging at the "Blistered" HOPG for Hydrazine Oxidation. We first consider an area (40 μm × 30 μm) of an electrochemically-treated HOPG surface, consisting of blisters formed where two or more grains meet. The SECCM voltammetric scan regime provides a series of potential-resolved images of I_{EC} at a set of *x*-*y* coordinates from which individual electrochemical (current) maps, at a given potential, can be extracted, or alternatively a movie of current varying with potential can be created. Figures 5a shows a current map at the most positive potential obtained from the SECCM-LSV movie file (Movie S2) in the Supporting Information which contains 191 images (336 pixels), one image every 2.56 mV, with the potential scanned from 0.45 V_{RHE} to 2.35 V_{RHE}. FE-SEM performed after SECCM imaging showed residues from the SECCM meniscus were left on the surface which had fairly consistent shape and size (Figure 5b), from which one can deduce that each measurement has a very similar local working electrode area. By coupling the SECCM measurements with FE-SEM applied to the same area, a detailed correlation of structure with electrocatalytic properties is revealed. The immediate and striking observation is that the electrochemical map in Figure 5a shows relatively high electrochemical activity at the blisters presented along the grain boundaries (region 1), as compared to the basal plane area (region 2).

To analyze the electrochemical behavior in detail, raw LSV data were extracted from two regions, 1 and 2 (Figures 5c), with LSVs from 5 individual pixels in each area (black), along with the resulting average LSV for each area (red). At a potential of 1.5 V_{RHE}, the peak current for hydrazine electro-oxidation in the blister (region 1) is ca. 1.3 nA. This current is significantly enhanced compared with the basal plane (region 2) which exhibits a peak current of ca. 0.5 nA at a much higher overpotential, ca. 2.05 V_{RHE}. Furthermore, the onset potential for hydrazine electro-oxidation at a blister (ca. 0.8 V_{RHE}) is significantly shifted to a more cathodic potential when

compared to voltammetry performed at the basal plane (ca. 1.6 V_{RHE}), indicating that the blister has greatly enhanced electrocatalytic activity for the electro-oxidation of hydrazine. Note that the limiting current is higher for the blistered graphite, as compared to a standard gold electrode in the same SECCM configuration (Supporting Information, section S1). Furthermore, SECCM voltammetry at the basal graphite surface gives a limiting current similar to gold (albeit shifted catholically by a large value). The higher current magnitude at the blister, is most likely due to the electrowetting of the substrate by the meniscus during ions intercalation/deintercalation, driven by the applied potential.[42] Interestingly, however, the electroactivity of the blistered region lies between that of the gold electrode and basal plane graphite, highlighting how simple surface modification can impart significant electrocatalytic effects.

A Tafel map (Figure 5d) was obtained to highlight the different kinetic regimes across the treated HOPG surface. The voltammetric data were analyzed in the potential intervals from 0.65 to 1.10 V (blistered region) and 1.40 to 1.70 V (basal plane region) corresponding to the foot of the wave, where mass transport and, as such, concentration polarization could be neglected in each case. The Tafel slope was in the range 100 – 180 mV/decade (region 1) and 250 – 400 mV/decade (region 2), as shown in Figure 5e. The Tafel slopes of the blistered region are superior to alternative carbon-based electrode catalyst, such as polypyrrole[55] or curcumin modified multi-walled carbon nanotubes[56] on a glassy carbon support. The charge transfer coefficient, α, was 0.33 – 0.59 in the blistered region which was determined from the Tafel slope, indicating a, more or less, one-electron process in the rate determining step, followed by processes amounting to the transfer of a further three electrons to give N_2 as a final product:[57, 58]

$$N_2H_5^+ \rightarrow N_2H_3(ads) + 2H^+ + e^- \quad (2)$$

$$N_2H_3(ads) \rightarrow N_2 + 3H^+ + 3e^- \quad (3)$$

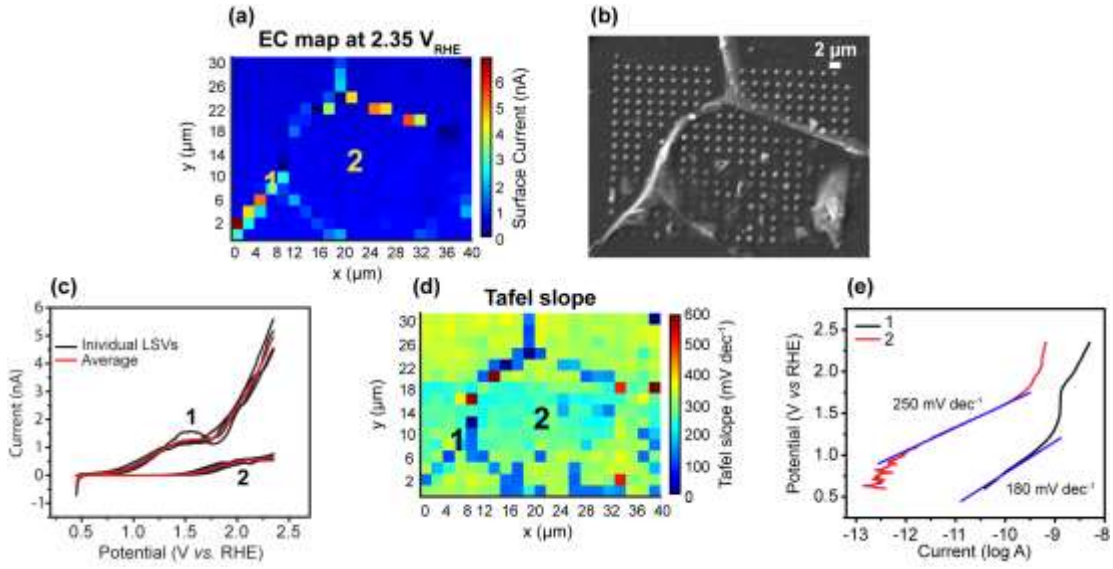

Figure 5. Electrochemical map of the modified HOPG substrate at (a) 2.35 V_{RHE} (5 mM N_2H_4). (b) FE-SEM image after SECCM imaging showing the locations of the individual pixels. (c) Individual LSVs (black, n = 5) and averaged LSV (red) for different regions marked in (a). (d) Tafel map (mV per decade) determined using data from 0.65 > E_s > 1.10 V_{RHE} (blister) and 1.40 > E_s > 1.70 V_{RHE} (basal plane). (e) Example Tafel plots highlighting the difference between regions 1 and 2 of (d).

To investigate further the influence of the HOPG structure on hydrazine oxidation, SECCM imaging was performed in a different area (40 μm × 44 μm) of an acid modified HOPG sample, comprising of small blisters as well as a relatively large blister along the grain boundaries. The current map in Figure 6a was extracted from an SECCM-LSV movie file (Supporting Information, Movie S3) in which the potential was scanned from 0.45 V_{RHE} to 2.1 V_{RHE} at each pixel (483 pixels with a hopping distance of 2 μm, Figure 6b). Strikingly, the electrochemical map, shows high activity at the blisters present along the grain boundaries with higher activity, particularly noticeable at the circumference of the large spherical blister (Figure 6b). Raw LSV data for the hydrazine oxidation were extracted at two pixels, spot 1 and spot 2, (Figures 6c). At a potential of

1.5 V_{RHE}, the peak current of the hydrazine electro-oxidation was ca. 5.4 nA (spot 1) and ca. 1.8 nA (spot 2). These result reveals heterogeneous electroactivity within the blister structure, with the highest activity attributed to the blister edge.

For comparison, Figures 6d and 6e show individual LSVs (n = 5), and the averaged response for regions A and B, respectively. The electrochemical behavior of the center of the blister (region A) is similar to the basal plane (region B), and displays low activity compared to the much more active regions of the blisters. Tafel analysis was performed on the SECCM scanned area and the resulting Tafel map is shown in Figure 6f. The analysis was in the potential range from 0.75 to 1.05 V (active region) and 0.90 to 1.30 V (less active region). The Tafel slope was 96±1 mV/decade (spot 1), 160±2 mV/decade (spot 2), and in the range 250 – 450 mV/decade (region A and B), with typical Tafel plots shown in Figure 6g. These data again reveal the power of the SECCM voltammetric mode to highlight key areas of activity on an electrocatalytic surface and, in this case, to even pinpoint differences in activity within blisters.

At pH 7.4, hydrazine (pKa = 8.1)[59] is largely protonated and, the blistered region has a high density of negatively charged electrochemically formed graphite oxide film evident from the broader *G*-band (Figure 4b(iv)) and oxygen groups (–COOH, –OH, –CHO) formed during potential cycling in acid.[60] These groups on the modified graphite surface can act as potential sites to adsorb active species, leading to enhanced electron transfer kinetics.[61] Further, the more disordered nature of the blister (increased *D*-band in Figure 4a(vi) and 4b(vi)) compared to the basal surface, leads to more ready ion-solvent intercalation during electrocatalysis, which could be important for improving the electrochemical activity. It should further be pointed out that N_2 nanobubbles can be formed during N_2H_4 electrooxidation and block the electrode surface.[62] The porous structure of blistered regions may aid the evolution of N_2 nanobubbles, resulting in an

enhancement of electrochemical activity. Finally, and significantly, the electronic properties of graphite change dramatically by the introduction of defects,[63] in particular, resulting in a high density of state near the Fermi level at defective graphite,[17, 52, 64] which would be expected to significantly enhance electrocatalysis.

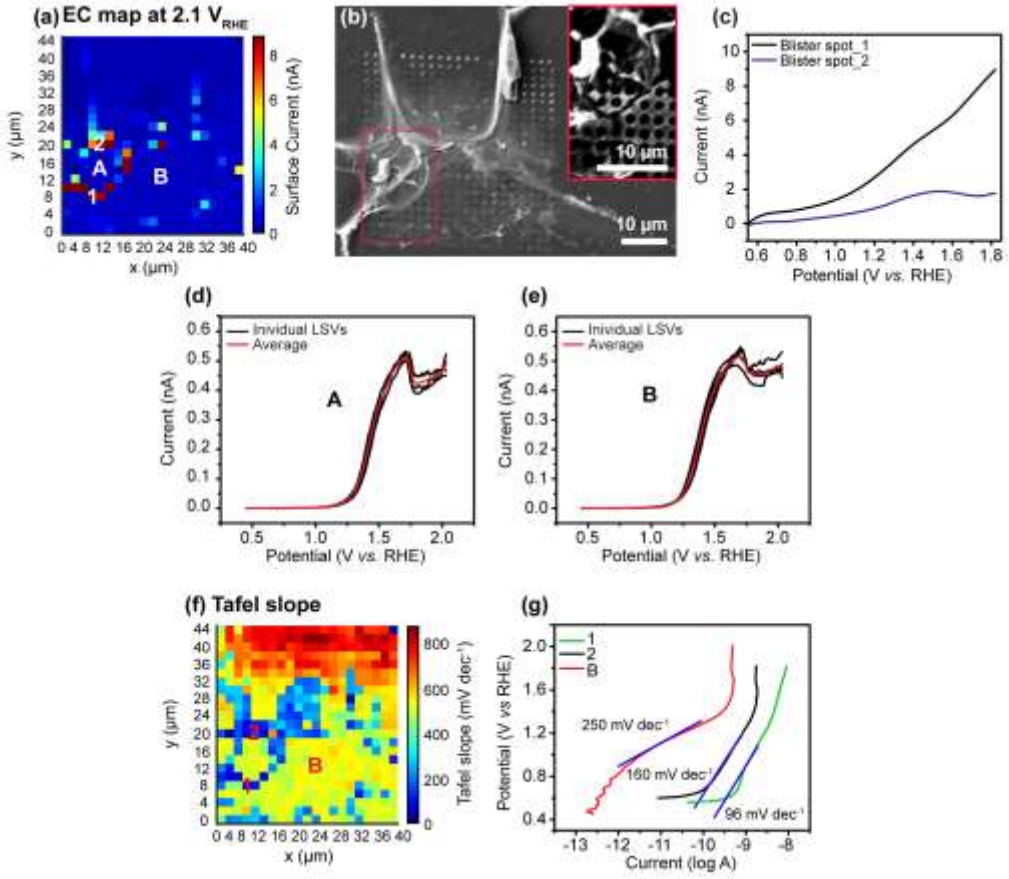

Figure 6. Electrochemical map of a modified HOPG substrate at (a) 2.1 V_{RHE} (5 mM N_2H_4) (b) FE-SEM image after SECCM imaging. LSV for different regions: (c) blister spots (1 and 2 in (a)), (d) Inner blister (A) (n = 5), and (e) basal plane (B) (n = 5). (f) Tafel map (mV per decade) determined using data from $0.75 > E_s > 1.05$ V_{RHE} (blister) and $0.90 > E_s > 1.30$ V_{RHE} (basal plane). (g) ExampleTafel plots from the labelled regions in (f).

CONCLUSIONS

In this study, we have shown that structural defects (surface blisters) which form on HOPG (at grain boundaries and step edges) during voltammetric cycling in 0.1 M $HClO_4$ can be readily characterized by FE-SEM and Raman microscopy. These structures show considerable electrocatalytic activity compared to basal HOPG areas on the same surface, as revealed by SECCM imaging. The use of the LSV-SECCM approach, in the study of these surface features, has enabled a potential sweep at every pixel of the scanned area to be performed, providing detailed information of microscopic activity. The extensive data sets produced have allowed us to observe an earlier onset potential, higher peak current, and smaller Tafel slope at the blistered area, all of which are indicative of enhanced electrocatalysis compared to the basal plane.

Several factors need to be considered to explain the dramatic effect of HOPG blisters on hydrazine electro-oxidation. These include enhanced adsorption of protonated hydrazine at the defect sites, the hollow nature of the blistered graphite that allows ion-solvent intercalation/de-intercalation during the electrocatalytic reaction, and the porous structure of the blistered region that would be less susceptible to N_2 nanobubbles blocking access to the surface. Overall, the results show that electrochemistry is a powerful tool for engineering the surface properties of graphite to make an effective electrocatalyst, and that state of the art electrochemical imaging, in combination with other microscopy techniques allows detailed correlations between structure and activity to be drawn and explained.

Supporting Information. S1. Linear sweep voltammograms (LSVs) of hydrazine oxidation at a gold electrode in a scanning electrochemical cell microscopy (SECCM) setup. S2. Electrochemical current (I_{EC}) movie of hydrazine oxidation area 1; S3. Electrochemical current (I_{EC}) movie of hydrazine oxidation area 2.

Notes

The authors declare no competing financial interests.

ACKNOWLEDGMENT

This work was, in part, supported by a European Research Council award (ERC-2009-AdG 247143-QUANTIF) (P.R.U.), Endeavour Fellowship Programme (Australian Government) (C.L.B.), and the EPSRC through the MOAC DTC, Grant No. EP/F500378/1 (D.P.). The National Research Foundation of Korea is also acknowledged for support of Y.-R. Kim (2016R1C1B2011912). S.P.E. would like to thank the University of Warwick for funding through the award of a Chancellor's International Scholarship.

REFERENCES

1. Suntivich, J.; Gasteiger, H. A.; Yabuuchi, N.; Nakanishi, H.; Goodenough, J. B.; Shao-Horn, Y. Design Principles for Oxygen-Reduction Activity on Perovskite Oxide Catalysts for Fuel Cells and Metal-Air Batteries. *Nat. Chem.* **2011**, *3*, 546-550.

2. Chen, Z.; Higgins, D.; Yu, A.; Zhang, L.; Zhang, J. A Review on Non-Precious Metal Electrocatalysts for PEM Fuel Cells. *Energy Environ. Sci.* **2011**, *4*, 3167-3192.

3. Zheng, Y.; Jiao, Y.; Zhu, Y.; Li, L. H.; Han, Y.; Chen, Y.; Du, A.; Jaroniec, M.; Qiao, S. Z. Hydrogen Evolution by a Metal-Free Electrocatalyst. *Nat. Commun.* **2014**, *5*, 3783.

4. Li, C.; Han, X.; Cheng, F.; Hu, Y.; Chen, C.; Chen, J. Phase and Composition Controllable Synthesis of Cobalt Manganese Spinel Nanoparticles towards Efficient Oxygen Electrocatalysis. *Nat. Commun.* **2015**, *6*, 7345.

5. Sahraie, N. R.; Kramm, U. I.; Steinberg, J.; Zhang, Y.; Thomas, A.; Reier, T.; Paraknowitsch, J.-P.; Strasser, P. Quantifying the Density and Utilization of Active Sites in Non-Precious Metal Oxygen Electroreduction Catalysts. *Nat. Commun.* **2015**, *6*, 8618.

6. Wang, H.; Lee, H.-W.; Deng, Y.; Lu, Z.; Hsu, P.-C.; Liu, Y.; Lin, D.; Cui, Y. Bifunctional Non-Noble Metal Oxide Nanoparticle Electrocatalysts through Lithium-Induced Conversion for Overall Water Splitting. *Nat. Commun.* **2015**, *6*, 7261.

7. Zhang, J.; Li, H.; Guo, P.; Ma, H.; Zhao, X. S. Rational Design of Graphitic Carbon Based Nanostructures for Advanced Electrocatalysis. *J. Mater. Chem. A* **2016**, *4*, 8497-8511.

8. Novoselov, K. S. Nobel Lecture: Graphene: Materials in the Flatland. *Rev. Mod. Phys.* **2011**, *83*, 837-849.

9. Planeix, J. M.; Coustel, N.; Coq, B.; Brotons, V.; Kumbhar, P. S.; Dutartre, R.; Geneste, P.; Bernier, P.; Ajayan, P. M. Application of Carbon Nanotubes as Supports in Heterogeneous Catalysis. *J. Am. Chem. Soc.* **1994**, *116*, 7935-7936.

10. Trogadas, P.; Fuller, T. F.; Strasser, P. Carbon as Catalyst and Support for Electrochemical Energy Conversion. *Carbon* **2014**, *75*, 5-42.

11. Zhao, Y.; Nakamura, R.; Kamiya, K.; Nakanishi, S.; Hashimoto, K. Nitrogen-Doped Carbon Nanomaterials as Non-Metal Electrocatalysts for Water Oxidation. *Nat. Commun.* **2013**, *4*, 2390.

12. Zhao, J.; Deng, Q.; Bachmatiuk, A.; Sandeep, G.; Popov, A.; Eckert, J.; Ruemmeli, M. H. Free-Standing Single-Atom-Thick Iron Membranes Suspended in Graphene Pores. *Science* **2014**, *343*, 1228-1232.

13. Dai, L.; Xue, Y.; Qu, L.; Choi, H.-J.; Baek, J.-B. Metal-Free Catalysts for Oxygen Reduction Reaction. *Chem. Rev.* **2015**, *115*, 4823-4892.

14. Gao, C.; Guo, Z.; Liu, J.-H.; Huang, X.-J. The New Age of Carbon Nanotubes: An Updated Review of Functionalized Carbon Nanotubes in Electrochemical Sensors. *Nanoscale* **2012**, *4*, 1948-1963.

15. Balasubramanian, K.; Burghard, M. Chemically Functionalized Carbon Nanotubes. *Small* **2005**, *1*, 180-192.

16. Dudin, P. V.; Snowden, M. E.; Macpherson, J. V.; Unwin, P. R. Electrochemistry at Nanoscale Electrodes: Individual Single-Walled Carbon Nanotubes (SWNTs) and SWNT-Templated Metal Nanowires. *ACS Nano* **2011**, *5*, 10017-10025.

17. Unwin, P. R.; Güell, A. G.; Zhang, G. Nanoscale Electrochemistry of Sp^2 Carbon Materials: From Graphite and Graphene to Carbon Nanotubes. *Acc. Chem. Res.* **2016**, 49, 2041–2048

18. Zhang, G.; Cuharuc, A. S.; Güell, A. G.; Unwin, P. R. Electrochemistry at Highly Oriented Pyrolytic Graphite (HOPG): Lower Limit for the Kinetics of Outer-Sphere Redox Processes and General Implications for Electron Transfer Models. *Phys. Chem. Chem. Phys.* **2015**, *17*, 11827-11838.

19. Zhang, G. H.; Kirkman, P. M.; Patel, A. N.; Cuharuc, A. S.; McKelvey, K.; Unwin, P. R. Molecular Functionalization of Graphite Surfaces: Basal Plane Versus Step Edge Electrochemical Activity. *J. Am. Chem. Soc.* **2014**, *136*, 11444-11451.

20. Patel, A. N.; McKelvey, K.; Unwin, P. R. Nanoscale Electrochemical Patterning Reveals the Active Sites for Catechol Oxidation at Graphite Surfaces. *J. Am. Chem. Soc.* **2012**, *134*, 20246-20249.

21. Patel, A. N.; Collignon, M. G.; O'Connell, M. A.; Hung, W. O. Y.; McKelvey, K.; Macpherson, J. V.; Unwin, P. R. A New View of Electrochemistry at Highly Oriented Pyrolytic Graphite. *J. Am. Chem. Soc.* **2012**, *134*, 20117-20130.

22. Wang, H.; Maiyalagan, T.; Wang, X. Review on Recent Progress in Nitrogen-Doped Graphene: Synthesis, Characterization, and Its Potential Applications. *ACS Catal.* **2012**, *2*, 781-794.

23. Panchokarla, L. S.; Subrahmanyam, K. S.; Saha, S. K.; Govindaraj, A.; Krishnamurthy, H. R.; Waghmare, U. V.; Rao, C. N. R. Synthesis, Structure, and Properties of Boron- and Nitrogen-Doped Graphene. *Adv. Mater.* **2009**, *21*, 4726-4730.

24. Yang, Z.; Yao, Z.; Li, G.; Fang, G.; Nie, H.; Liu, Z.; Zhou, X.; Chen, X. a.; Huang, S. Sulfur-Doped Graphene as an Efficient Metal-Free Cathode Catalyst for Oxygen Reduction. *ACS Nano* **2012**, *6*, 205-211.

25. Liu, Z.-W.; Peng, F.; Wang, H.-J.; Yu, H.; Zheng, W.-X.; Yang, J. Phosphorus-Doped Graphite Layers with High Electrocatalytic Activity for the O_2 Reduction in an Alkaline Medium. *Angew. Chem. Int. Ed.* **2011**, *50*, 3257-3261.

26. Delamar, M.; Hitmi, R.; Pinson, J.; Saveant, J. M. Covalent Modification of Carbon Surfaces by Grafting of Functionalized Aryl Radicals Produced from Electrochemical Reduction of Diazonium Salts. *J. Am. Chem. Soc.* **1992**, *114*, 5883-5884.

27. Greenwood, J.; Phan, T. H.; Fujita, Y.; Li, Z.; Ivasenko, O.; Vanderlinden, W.; Van Gorp, H.; Frederickx, W.; Lu, G.; Tahara, K.; Tobe, Y.; Uji-i, H.; Mertens, S. F. L.; De Feyter, S. Covalent Modification of Graphene and Graphite Using Diazonium Chemistry: Tunable Grafting and Nanomanipulation. *ACS Nano* **2015**, *9*, 5520-5535.

28. Byers, J. C.; Güell, A. G.; Unwin, P. R. Nanoscale Electrocatalysis: Visualizing Oxygen Reduction at Pristine, Kinked, and Oxidized Sites on Individual Carbon Nanotubes. *J. Am. Chem. Soc.* **2014**, *136*, 11252-11255.

29. Shen, A.; Zou, Y.; Wang, Q.; Dryfe, R. A. W.; Huang, X.; Dou, S.; Dai, L.; Wang, S. Oxygen Reduction Reaction in a Droplet on Graphite: Direct Evidence That the Edge Is More Active Than the Basal Plane. *Angew. Chem. Int. Ed.* **2014**, *53*, 10804-10808.

30. Hathcock, K. W.; Brumfield, J. C.; Goss, C. A.; Irene, E. A.; Murray, R. W. Incipient Electrochemical Oxidation of Highly Oriented Pyrolytic-Graphite: Correlation between Surface Blistering and Electrolyte Anion Intercalation. *Anal. Chem.* **1995**, *67*, 2201-2206.

31. Goss, C. A.; Brumfield, J. C.; Irene, E. A.; Murray, R. W. Imaging the Incipient Electrochemical Oxidation of Highly Oriented Pyrolytic Graphite. *Anal. Chem.* **1993**, *65*, 1378-1389.

32. Alliata, D.; Kotz, R.; Haas, O.; Siegenthaler, H. In Situ AFM Study of Interlayer Spacing During Anion Intercalation into HOPG in Aqueous Electrolyte. *Langmuir* **1999**, *15*, 8483-8489.

33. Sanabria-Chinchilla, J.; Asazawa, K.; Sakamoto, T.; Yamada, K.; Tanaka, H.; Strasser, P. Noble Metal-Free Hydrazine Fuel Cell Catalysts: EPOC Effect in Competing Chemical and Electrochemical Reaction Pathways. *J. Am. Chem. Soc.* **2011**, *133*, 5425-5431.

34. Zhou, W. H.; Xu, L.; Wu, M. J.; Xu, L. J.; Wang, E. Determination of Hydrazines by Capillary Zone Electrophoresis with Amperometric Detection at a Platinum Particle-Modified Carbon-Fiber Microelectrode. *Anal. Chim. Acta* **1994**, *299*, 189-194.

35. Channon, R. B.; Joseph, M. B.; Bitziou, E.; Bristow, A. W. T.; Ray, A. D.; Macpherson, J. V. Electrochemical Flow Injection Analysis of Hydrazine in an Excess of an Active Pharmaceutical Ingredient: Achieving Pharmaceutical Detection Limits Electrochemically. *Anal. Chem.* **2015**, *87*, 10064-10071.

36. Chen, C.-H.; Jacobse, L.; McKelvey, K.; Lai, S. C. S.; Koper, M. T. M.; Unwin, P. R. Voltammetric Scanning Electrochemical Cell Microscopy: Dynamic Imaging of Hydrazine Electro-Oxidation on Platinum Electrodes. *Anal. Chem.* **2015**, *87*, 5782-5789.

37. Ebejer, N.; Güell, A. G.; Lai, S. C. S.; McKelvey, K.; Snowden, M. E.; Unwin, P. R. Scanning Electrochemical Cell Microscopy: A Versatile Technique for Nanoscale Electrochemistry and Functional Imaging. *Annu. Rev. Anal. Chem.* **2013**, *6*, 329-351.

38. Aaronson, B. D. B.; Chen, C.-H.; Li, H.; Koper, M. T. M.; Lai, S. C. S.; Unwin, P. R. Pseudo-Single-Crystal Electrochemistry on Polycrystalline Electrodes: Visualizing Activity at Grains and Grain Boundaries on Platinum for the Fe^{2+}/Fe^{3+} Redox Reaction. *J. Am. Chem. Soc.* **2013**, *135*, 3873-3880.

39. Güell, A. G.; Cuharuc, A. S.; Kim, Y.-R.; Zhang, G.; Tan, S.-Y.; Ebejer, N.; Unwin, P. R. Redox-Dependent Spatially Resolved Electrochemistry at Graphene and Graphite Step Edges. *ACS Nano* **2015**, *9*, 3558-3571.

40. Güell, A. G.; Meadows, K. E.; Dudin, P. V.; Ebejer, N.; Macpherson, J. V.; Unwin, P. R. Mapping Nanoscale Electrochemistry of Individual Single-Walled Carbon Nanotubes. *Nano Lett.* **2014**, *14*, 220-224.

41. Vasile, M. J.; Enke, C. G. The Preparation and Thermodynamic Properties of a Palladium-Hydrogen Electrode. *J. Electrochem. Soc.* **1965**, *112*, 865-870.

42. Zhang, G.; Walker, M.; Unwin, P. R. Low-Voltage Voltammetric Electrowetting of Graphite Surfaces by Ion Intercalation/Deintercalation. *Langmuir* **2016**, *32*, 7476-7484.

43. Bertoncello, P.; Edgeworth, J. P.; Macpherson, J. V.; Unwin, P. R. Trace Level Cyclic Voltammetry Facilitated by Single-Walled Carbon Nanotube Network Electrodes. *J. Am. Chem. Soc.* **2007**, *129*, 10982-10983.

44. E, S. P.; Liu, D.; Lazenby, R. A.; Sloan, J.; Vidotti, M.; Macpherson, J. V.; Unwin, P. R. Electrodeposition of Nickel Hydroxide Nanoparticles on Carbon Nanotube Electrodes: Correlation of Particle Crystallography with Electrocatalytic Properties. *J. Phys. Chem. C* **2016**, *120*, 16059-16068.

45. Ebejer, N.; Schnippering, M.; Colburn, A. W.; Edwards, M. A.; Unwin, P. R. Localized High Resolution Electrochemistry and Multifunctional Imaging: Scanning Electrochemical Cell Microscopy. *Anal. Chem.* **2010**, *82*, 9141-9145.

46. Alsmeyer, D. C.; McCreery, R. L. In Situ Raman Monitoring of Electrochemical Graphite-Intercalation and Lattice Damage in Mild Aqueous Acids. *Anal. Chem.* **1992**, *64*, 1528-1533.

47. Dresselhaus, M. S.; Dresselhaus, G. Intercalation Compounds of Graphite. *Adv. Phys.* **1981**, *30*, 139-326.

48. Schnyder, B.; Alliata, D.; Kotz, R.; Siegenthaler, H. Electrochemical Intercalation of Perchlorate Ions in HOPG: An SFM/LFM and XPS Study. *Appl. Surf. Sci.* **2001**, *173*, 221-232.

49. Choo, H. S.; Kinumoto, T.; Nose, M.; Miyazaki, K.; Abe, T.; Ogumi, Z. Electrochemical Oxidation of Highly Oriented Pyrolytic Graphite During Potential Cycling in Sulfuric Acid Solution. *J. Power Sources* **2008**, *185*, 740-746.

50. Dresselhaus, M. S.; Jorio, A.; Souza Filho, A. G.; Saito, R. Defect Characterization in Graphene and Carbon Nanotubes Using Raman Spectroscopy. *Phil. Trans. R. Soc. A* **2010**, *368*, 5355-5377.

51. Maeda, Y.; Okemoto, Y.; Inagaki, M. Electrochemical Formation of Graphite-Sulfuric Acid Intercalation Compounds on Carbon-Fibers. *J. Electrochem. Soc.* **1985**, *132*, 2369-2372.

52. Zhong, J.-H.; Zhang, J.; Jin, X.; Liu, J.-Y.; Li, Q.; Li, M.-H.; Cai, W.; Wu, D.-Y.; Zhan, D.; Ren, B. Quantitative Correlation between Defect Density and Heterogeneous Electron Transfer Rate of Single Layer Graphene. *J. Am. Chem. Soc.* **2014**, *136*, 16609-16617.

53. Alsmeyer, Y. W.; McCreery, R. L. Surface-Enhanced Raman-Spectroscopy of Carbon Electrode Surfaces Following Silver Electrodeposition. *Anal. Chem.* **1991**, *63*, 1289-1295.

54. McCreery, R. L. Advanced Carbon Electrode Materials for Molecular Electrochemistry. *Chem. Rev.* **2008**, *108*, 2646-2687.

55. Majidi, M. R.; Jouyban, A.; Asadpour-Zeynali, K. Electrocatalytic Oxidation of Hydrazine at Overoxidized Polypyrrole Film Modified Glassy Carbon Electrode. *Electrochim. Acta* **2007**, *52*, 6248-6253.

56. Zheng, L.; Song, J. F. Curcumin Multi-Wall Carbon Nanotubes Modified Glassy Carbon Electrode and Its Electrocatalytic Activity towards Oxidation of Hydrazine. *Sens. Actuator B-Chem.* **2009**, *135*, 650-655.

57. Harrison, J. A.; Khan, Z. A. Oxidation of Hydrazine on Platinum in Acid Solution. *J. Electroanal. Chem.* **1970**, *28*, 131-138.

58. Harrison, J. A.; Khan, Z. A., Oxidation of Hydrazine in Alkaline Solution at Platinum and Mercury. *J. Electroanal. Chem.* **1970**, *26*, 1-11.

59. Zhang, C. H.; Wang, G. F.; Ji, Y. L.; Liu, M.; Feng, Y. H.; Zhang, Z. D.; Fang, B. Enhancement in Analytical Hydrazine Based on Gold Nanoparticles Deposited on ZnO-MWCNTS Films. *Sens. Actuator B-Chem.* **2010**, *150*, 247-253.

60. E, S. P.; Miller, T. S.; Macpherson, J. V.; Unwin, P. R. Controlled Functionalisation of Single-Walled Carbon Nanotube Network Electrodes for the Enhanced Voltammetric Detection of Dopamine. *Phys. Chem. Chem. Phys.* **2015**, *17*, 26394-26402.

61. Su, C.; Loh, K. P. Carbocatalysts: Graphene Oxide and Its Derivatives. *Acc. Chem. Res.* **2013**, *46*, 2275-2285.

62. Chen, Q.; Wiedenroth, H. S.; German, S. R.; White, H. S. Electrochemical Nucleation of Stable N2 Nanobubbles at Pt Nanoelectrodes. *J. Am. Chem. Soc.* **2015**, *137*, 12064-12069.

63. Banhart, F.; Kotakoski, J.; Krasheninnikov, A. V. Structural Defects in Graphene. *ACS Nano* **2011**, *5*, 26-41.

64. Deng, D.; Novoselov, K. S.; Fu, Q.; Zheng, N.; Tian, Z.; Bao, X. Catalysis with Two-Dimensional Materials and Their Heterostructures. *Nat. Nanotechnol.* **2016**, *11*, 218-230.

Table of Contents Graphic